Quantitative Fluorescent Speckle Microscopy of Cytoskeleton Dynamics

Gaudenz Danuser and Clare M. Waterman-Storer

Department of Cell Biology, The Scripps Research Institute, La Jolla, California 92037; email: gdanuser@scripps.edu, waterman@scripps.edu

Annu. Rev. Biophys. Biomol. Struct. 2006. 35:361–87

The *Annual Review of Biophysics and Biomolecular Structure* is online at biophys.annualreviews.org

doi: 10.1146/annurev.biophys.35.040405.102114

1056-8700/06/0609-0361$20.00

Key Words

computer vision, particle tracking, actin, microtubule, focal adhesion

Abstract

Fluorescent speckle microscopy (FSM) is a technology used to analyze the dynamics of macromolecular assemblies in vivo and in vitro. Speckle formation by random association of fluorophores with a macromolecular structure was originally discovered for microtubules. Since then FSM has been expanded to study other cytoskeleton and cytoskeleton-binding proteins. Specialized software has been developed to convert the stochastic speckle image signal into spatiotemporal maps of polymer transport and turnover in living cells. These maps serve as a unique quantitative readout of the dynamic steady state of the cytoskeleton and its responses to molecular and genetic interventions, allowing a systematic study of the mechanisms of cytoskeleton regulation and its effect on cell function. Here, we explain the principles of FSM imaging and signal analysis, outline the biological questions and corresponding methodological advances that have led to the current state of FSM, and give a glimpse of new FSM modalities under development.

Contents

INTRODUCTION

Fluorescent speckle microscopy (FSM): imaging of speckle signals using the different modalities of fluorescence light microscopy

Fluorescent speckle microscopy (FSM) is a method used to analyze the movement and assembly/disassembly dynamics of macromolecular structures in vivo and in vitro (58). As reviewed in References 10 and 57, FSM is derived from the principles of fluorescent analog cytochemistry. There, purified protein is covalently linked to a fluorophore and microinjected or expressed as a GFP fusion in living cells. Fluorescent protein that incorporates into cellular structures is then visualized by epifluorescence light microscopy (40, 54). This classic approach has yielded much information about protein localization and the dynamics of macromolecular assemblies in cells but has been limited in its ability to report protein dynamics because of inherently high background fluorescence from unincorporated and out-of-focus incorporated fluorescent subunits. In addition it is often impossible to detect movement or turnover

of subunits within assemblies because of the uniform fluorescent labeling of structures. These problems have been alleviated by the use of laser photobleaching and photoactivation of fluorescence to mark structures in limited cell areas and measure the movement and turnover of subunits in the marked region at steady state (25, 31, 46, 52, 53, 66). Similar to these techniques is the ratiometric method of fluorescence localization after photobleaching (FLAP) (12, 70). FSM provides the same information as these photomarking techniques. In addition, it delivers simultaneous kinetic data in large areas of the cell, offering the capability to detect nonsteady-state molecular dynamics within assemblies at high spatial and temporal resolution. FSM also reduces out-of-focus fluorescence in images and improves the visibility of fluorescently labeled structures and their dynamics in three-dimensional polymer arrays such as the mitotic spindle (27, 28, 59).

In its initial development, FSM utilized wide-field epifluorescence light microscopy and digital imaging with a sensitive, low-noise cooled charge-coupled-device (CCD) camera and was applied to the study of assembly dynamics and movement of microtubules (60). Since then FSM has been transferred to confocal and total internal reflection fluorescence microscopes (1, 2, 16, 27) and has been applied to new biological problems in vivo and in vitro. A critical step in advancing FSM to become a routine method for measuring cytoskeleton flow and turnover was the development of fully automated computer-based tracking and statistical analysis of speckle dynamics. Recently, these models for speckle image analysis have been expanded to infer the transient coupling between two protein assemblies and to probe viscoelastic properties of polymer networks.

In this paper, we review the principles of speckle formation and describe the imaging and analytical requirements for FSM to become a quantitative technique. We heavily rely on FSM data of actin cytoskeleton dynamics in epithelial cell migration, where we believe the integration of FSM imaging and computational image analysis has been brought to the most sophisticated level. The value of FSM as a general technique for the analysis of macromolecular assemblies is documented in a comprehensive table (Table S1; follow the Supplemental Material link from the Annual Reviews home page at **http://www.annualreviews.org**). The paper concludes with an outlook on our newest developments of FSM for the measurement of cytoskeleton-adhesion coupling and of material properties of actin filament networks.

MAP: microtubule-associated protein

Fluorescent speckle: random, diffraction-limited intensity peak in the image signal significantly brighter than the neighboring signal

PRINCIPLES OF SPECKLE IMAGE FORMATION

Stochastic Association of Fluorophores with Microtubules

FSM was discovered by accident when it was noticed in high-resolution images of cells injected with X-rhodamine tubulin that some microtubules exhibited variations in fluorescence intensity along their lattices, i.e., they looked speckled (**Figure 1*a*,*b***) (60). There were several possible interpretations of such images: (*a*) the fluorescent tubulin could preferentially associate with itself, forming bright oligomers or aggregates on the microtubule; (*b*) cellular factors such as organelles or microtubule-associated proteins (MAPs) could be bound to the microtubule and "mask" or quench the fluorescence of some regions; or (*c*) variations in the number of fluorescent tubulin subunits in each resolution-limited image region along the microtubule could occur as the microtubule assembled from a pool of labeled and unlabeled dimers (61).

We discounted the hypothesis that speckles were generated by fluorescent aggregates by showing that labeled tubulin dimers sediment similarly to unlabeled purified dimers in an analytical ultracentrifugation assay. Next, we showed that fluorescent speckle patterns

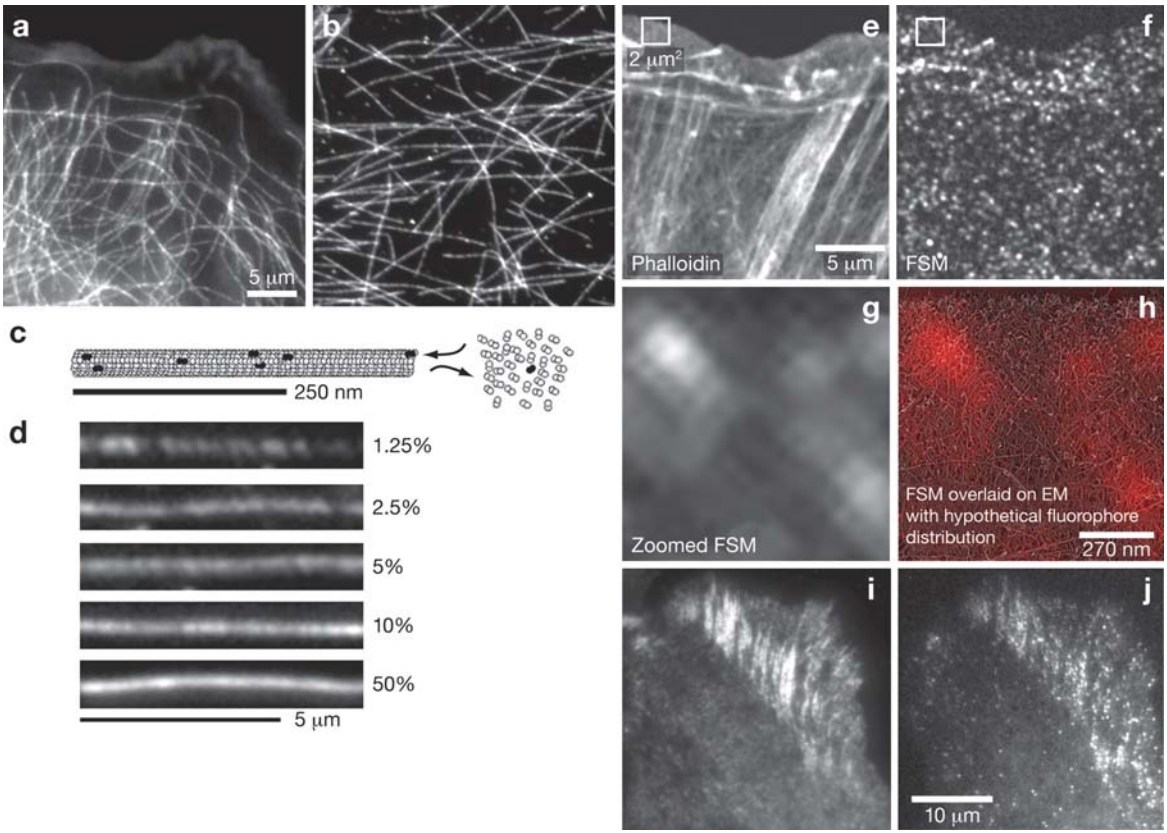

Figure 1

Speckle formation in microtubule and actin cytoskeletal polymers and focal adhesion (FAs). (*a*, *b*) Comparison of random speckle pattern of fluorescence along microtubules for (*a*) a living epithelial cell microinjected with X-rhodamine-labeled tubulin and for (*b*) microtubules assembled in vitro from 5% X-rhodamine-labeled tubulin. Scale bar: 5 μm. (*c*) Model for fluorescent speckle pattern formation in a microtubule grown from a tubulin pool containing a small fraction of labeled dimers. (*d*) Dependence of speckle contrast on the fraction of labeled tubulin dimers. (*e*, *f*) Speckle formation in actin filament networks. An epithelial cell was microinjected with a low level of X-rhodamine-labeled actin, fixed, and stained with Alexa-488 phalloidin. (*e*) Phalloidin image showing the organization of actin filaments in amorphous filament networks and bundles. (*f*) In the single FSM image much of the structural information is lost, but time-lapse FSM series contain dynamic information of filament transport and turnover not accessible with higher-level labeling of the cytoskeleton. (*g*) Close-up of 2 μm × 2 μm window in panels *e* and *f*. (*h*) Colorized speckle signal overlaid onto a quick-freeze deep etch image of the same-sized region of the actin cytoskeleton in the leading edge of a fibroblast (kindly provided by Tatyana Svitkina) with hypothetical fluorophore distribution that could give rise to such speckle pattern. This indicates the scale of FSM compared with ultrastructure of the polymer network and illustrates that a small proportion of the total actin fluoresces and that fluorophores from different filaments contribute to the same speckle. (*i*, *j*) Low-level expression of GFP-tagged FA protein vinculin results in speckled FAs in TIRF images. A cell expressing GFP-vinculin was fixed and immunofluorescently stained with antibodies to (*i*) vinculin to reveal the position of FAs, which in the (*j*) GFP channel appear speckled because of the low level of incorporation of GFP-vinculin.

on microtubules assembled from purified tubulin in vitro were similar to those of microtubules in cells where MAPs and organelles are present (61). Thus, the most plausible explanation for speckle formation in microtubules was that variations existed in the number of fluorescent tubulin subunits in each resolution-limited image region along the microtubule.

To understand how speckles originated, we considered how the images of fluorescent microtubules were formed by the microscope (**Figure 1*c***). Microtubules assemble from α/β tubulin dimers into the 25-nm-diameter cylindrical wall such that there are 1625 dimers per micron (11). The final image results from a convolution of the fluorophore distribution along the microtubule with the point-spread function (PSF) of the microscope. For a two-dimensional treatment of the situation, the in-focus slice of the PSF is given by the Airy disk, for which the radius of the first ring with zero intensity amounts to $r = 0.61\ \lambda$ /NA (20). The parameters λ and NA denote the emission wavelength of the fluorophore and the numerical aperture of the objective lens, respectively. For X-rhodamine-labeled microtubules (620-nm emission), the radius of the Airy disk is 270 nm (NA = 1.4), which corresponds to 440 tubulin dimers. A given fraction of fluorescent dimers, f, produces a mean number of fluorescent dimers $n = 440 \times f$ per PSF. The speckle pattern along the microtubule is produced by variations in the number of fluorescent dimers per PSF relative to this mean. Thus, the contrast of the speckle pattern can be approximated by the ratio of the standard deviation and the mean of a binomial distribution with n elements: $c = \sqrt{n \cdot f \cdot (1 - f)}/(n \cdot f)$. This formula suggests that the contrast c increases with decreasing f and decreases with increasing n, indicating the requirement for optics with the highest NA possible. This behavior is illustrated in **Figure 1*d***. Microtubules assembled from pure tubulin containing 1.25% to 5% labeled dimers exhibit speckles of varying intensity along their length. Microtubules assembled from 10% to 50% labeled tubulin are evenly labeled.

In theory, optimal contrast is obtained where speckles are formed by a single fluorophore per Airy disk (55, 62). For a microtubule, 80% or more speckles arise from a single fluorophore when f is less than 0.1% (10). In practice, however, the lower bound for f is determined by two considerations: (*a*) Technologically, the noise level and sensitivity of the imaging system, instability of the microscope, and the dynamics of the observed process may all deteriorate feasibility of single fluorophore detection. (*b*) Experimentally, too-low fractions result in a very low density of speckles, i.e., in low spatiotemporal sampling of underlying dynamics. We have found by both theory and practice that it is often desirable to image speckles at fractions in the range of 0.5% to 2%. In this range speckles consist of three to eight fluorophores (10).

PSF: point spread function of the microscope

F-actin: filamentous (polymeric) actin

Stochastic Association of Fluorophores in Other Systems: The Platform Model for Speckle Formation

When cells are injected with low levels of fluorescently labeled actin and imaged at high resolution, actin-rich structures appear relatively evenly speckled and do not indicate the architectural organization of the cytoskeleton (**Figure 1*e*,*f***) (41, 51, 55, 58, 63). Similar images can also be obtained by expressing GFP-fused actin at a very low level (23, 55) or by injecting trace amounts of the labeled actin-binding molecule phalloidin (47, 69). In contrast to speckle formation in isolated microtubules, labeled actin subunits associate with a highly cross-linked three-dimensional network of actin filaments (F-actin) (34, 44, 45). The mesh size of an F-actin network in living cells is nearly always below the resolution limit of the light microscope (**Figure 1*g*,*b***). Consequently, unless f is kept extremely low so that only one fluorophore falls into the PSF volume (55), fluorescent speckles arise most

FA: focal adhesion

likely from subunits distributed across several filaments.

The same concept of speckle formation has been exploited to visualize molecules making up focal adhesions (FAs) (1). GFP-fusions to FA proteins, including vinculin, talin, paxilin, α-actinin, zyxin, or $\alpha_v$integrin (15), have been expressed in epithelial cells from crippled promoters to achieve very low levels. Labeled proteins assembling with endogenous, unlabeled proteins give FAs a speckled appearance (**Figure 1*i,j***). As with actin networks, speckles represent randomly distributed fluorescent FA proteins that are temporarily clustered in the FA complex within the three-dimensional volume of one PSF.

A speckle is thus defined as a diffraction-limited image region that is significantly higher in fluorophore concentration (reported by fluorescence intensity) than its neighboring diffraction-limited image regions. In addition, for a speckle signal to be detected, the contributing fluorescent molecules must be immobilized within the PSF volume for the 0.1 to 2 s exposure time required by most digital cameras to acquire the dim FSM image. In contrast, unbound, diffusible fluorescent molecules yield an evenly distributed background signal of significantly lower magnitude across the many pixels that the molecules visit during the exposure. In a high-resolution (~250 nm), high-magnification (100×) image, actin monomers move ~60 pixels s^{-1} (26). The concept of fluorophore immobilization leading to speckle formation was nicely demonstrated by Watanabe & Mitchison (55). Diffusible GFP expressed in cells at very low levels produced an even distribution of fluorescence, whereas a similar level of GFP-conjugated actin that incorporated into the cytoskeleton produced a speckled image. The same idea was pursued by Bulinski et al. (7) and by Kapoor & Mitchison (24). GFP chimera of the MAP ensconsin (7) and fluorescently tagged tetrameric kinesin motor Eg5 (24) were used to observe the transient binding of these molecules to microtubules in vitro and in vivo.

In summary, speckle signal formation occurs when one or a few fluorescently labeled molecules within a PSF volume associate with a molecular scaffold where no other fluorescent molecules are located. We refer to this scaffold as the speckle platform. Association with the platform occurs when labeled subunits completely incorporate into the platform, as with tubulin or actin, or when they bind to it, as in the case of cytoskeleton-binding proteins or FA molecules. The duration of association must be equal to or longer than the camera exposure of one frame in a time-lapse image sequence.

Naïve Interpretation of Speckle Dynamics

Following the platform model, one would expect the appearance of a speckle to correspond to the local association of subunits with the platform. Conversely, the disappearance of a speckle would mark the local dissociation of subunits. In other words, FSM allows, in principle, the direct kinetic measurement of subunit turnover in space and time via speckle lifetime analysis. In addition, once a speckle is formed, it may undergo motion that indicates the coordinated movement of labeled subunits on the platform and/or the movement of the platform itself.

Computational Models of Speckle Dynamics

The interpretation of speckle dynamics becomes significantly more complicated when individual speckles arise from fluorophores distributed over multiple polymers. To examine how speckle appearance and disappearance relate to the rates of assembly and disassembly of F-actin, we performed Monte Carlo simulations of fluorophore incorporation into growing and shrinking filaments in dense and branched networks and generated synthetic FSM time-lapse sequences (39). The first lesson we learned from this modeling was that the speckle density is independent of whether

the network assembles or disassembles; it depends only on how many Airy disks can be resolved per unit area, e.g., 1 μm^2. With NA = 1.4/100 × optics, this amounts to ~4 (approximately 2 × 2), as confirmed by **Figure 2*a***. The graph displays the mean speckle density from five simulations of a network that starts with no fluorophores, assembles for 120 s (inset: mean fluorescence intensity increases), and disassembles for 360 s (inset: mean fluorescence intensity decreases) at equal rates. The density does not change after saturation at 100 s and remains constant despite further addition of fluorophores for another 20 s. This suggests that monomer association can cause an equal number of speckle appearances and disappearances. The same holds in the opposite sense during network disassembly.

Whereas the NA of the optics defines the maximum number of resolvable speckles per unit area, the labeling ratio influences the speckle density indirectly. For multi-fluorophore speckles the ratio f is the main determinant of speckle contrast. When increasing the ratio the speckle density drops because the difference between the peak intensity of a speckle and its surroundings is no longer distinguishable from intensity fluctuations due to noise. Similarly, at labeling ratios where speckles represent the image of single fluorophores ($f < 0.1\%$), a further decrease of f reduces the speckle density proportionally. Across the optimal range of ratios for multi-fluorophore speckles ($0.5\% < f < 3\%$) the density is almost constant. These model predictions were largely confirmed experimentally by Adams et al. (1).

The reason for the constant speckle density in the range of $0.5\% < f < 3\%$ is illustrated in **Figure 2*b***. A speckle is defined as a local image intensity maximum significantly above the surrounding background. The critical intensity difference ΔI_{crit} depends on both the camera noise and the shot noise. The shot noise is by itself a function of the speckle intensity (39). Speckles may appear (speckle birth) for two reasons: the intensity of a local maximum gets brighter because of the association of fluorescent subunits, or the intensity of the surrounding background gets dimmer because of subunit dissociation in the neighborhood. In both cases a speckle birth is detected when the peak-to-background intensity difference exceeds ΔI_{crit}. Analogously, speckles may disappear (speckle death) either because of subunit dissociation in the location of a speckle or because of subunit association in the neighborhood.

Multi-fluorophore speckle: fluorescent speckle with contributions from several fluorophores

Statistical Analysis of Speckle Dynamics

With the classification scheme in **Figure 2*b***, speckles become time-specific, diffraction-limited probes of polymer network turnover. The change in foreground or background intensity that causes the birth or death of a speckle is, on average, proportional to the net number of subunits Δm added to or removed from the PSF volume between two frames. This defined an algorithm for the local measurement of network assembly or disassembly kinetics (39): (*a*) calculation of changes in foreground and background intensities. After detection of a speckle birth/death event, regression lines are fitted to the foreground and background intensities for one time point before, at, and after the event (**Figure 2*c***). Intensity values before birth and after death are extrapolated (39). The line fits provide two estimates a_f and a_b of the slopes of foreground and background intensity variation. They also yield the standard deviations $\sigma(a_f)$ and $\sigma(a_b)$ of the slopes, which are derived from the residuals of the intensity values to the regression line. Noisy data, poorly represented by the regression model, generate large values for σ; intensity values in perfect match with the model result in small values for σ. (*b*) Each of the two slopes is tested for statistical significance. Insignificant intensity changes are discarded. (*c*) If both foreground and background slopes are significant, the one with the higher significance (lower p-value) is selected as the cause of the event. In the example given in

Figure 2*c* the foreground slope has the higher significance. The magnitude of the more significant slope is recorded as the score of the birth/death event. If neither foreground nor background slope is statistically significant, no score is generated.

Score values represent instantiations of a random variable with an expectation value $\mu = \alpha\Delta m \cdot f$ and variance $\sigma^2 = \alpha^2\Delta m^2 \cdot f(1 - f)$, where α denotes the unknown intensity of one fluorophore. In addition, the scores are perturbed by noise. However, assuming that the net rate Δm remains constant for a small probing window, the intrinsic score variation and noise are approximately eliminated by averaging all scores falling into the window. The choice of the window size depends on the density of significant scores and the user's preference for spatial or temporal resolution. The larger the number of scores averaged by time integration, the less spatial averaging is required, and vice versa.

Figure 2*d* displays rates of actin assembly (red) and disassembly (green) of the actin

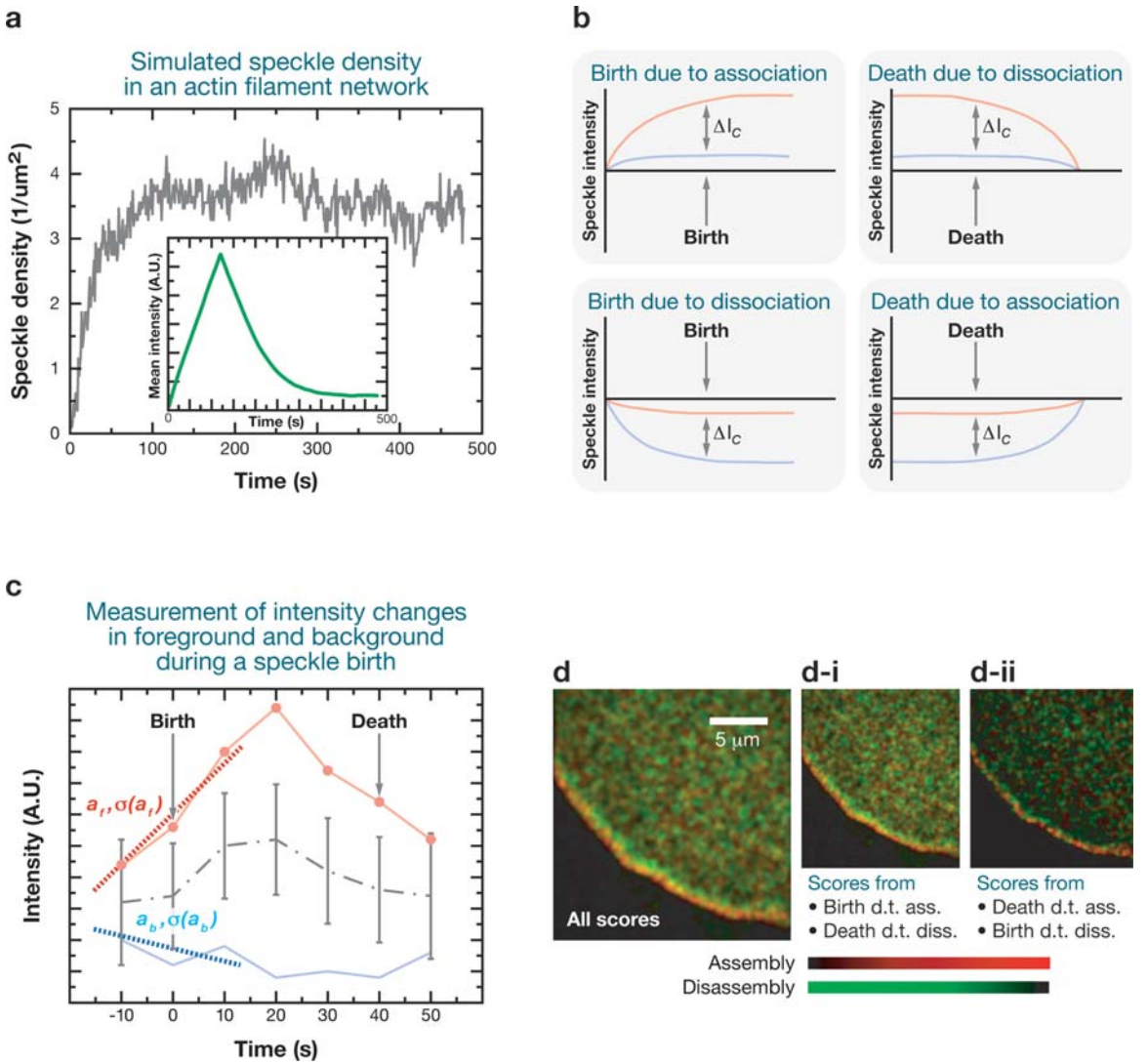

network at the edge of an epithelial cell. Here, score values were averaged over 10 min, reflecting the steady-state turnover. Animated maps resolved at 10-s intervals are provided as online supplementary material (movies M1 and M2; follow the Supplemental Material link from the Annual Reviews home page at **http://www.annualreviews.org**). The two smaller panels indicate the rate distributions calculated from scores extracted from speckle births due to monomer association and from speckle deaths due to monomer dissociation only (**Figure 2*d*-i**), and from births due to monomer dissociation and from deaths due to monomer association only (**Figure 2*d*-ii**). Both panels display the same distribution of loci of strong assembly (for example, the cell edge) and disassembly but at different event densities. **Figure 2*d*-i** corresponds to the naïve interpretation of speckle appearance and disappearance. These events contribute ~70% of all scores. The other ~30% of significant scores is related to the counterintuitive cases of speckle birth and death. Neglecting them would significantly reduce the sample size. How many intuitive versus counterintuitive cases occur depends on the fraction of labeled monomers. The lower the fraction, the fewer counterintuitive cases observed, with a lower boundary defined by the single-fluorophore speckle regime, in which all speckle appearances are due to monomer association and all disappearances are due to monomer dissociation.

Single-fluorophore speckle: fluorescent speckle that consists of an isolated fluorophore generating a detectable signal above background according to the definition of a fluorescent speckle

The processing of only short time intervals around speckle births and deaths focuses the analysis on image events that are more likely to have originated from monomer exchange rather than from intensity fluctuations due to image noise, bleaching, and in- and out-of-focus speckle motion. In addition, the algorithm rejects ~60% of all speckle birth and death events as insignificant (36), i.e., these events are not classifiable as induced by monomer exchange with the certainty the user chooses as the confidence level for the analysis. Bleaching affects all speckle scores and thus can be corrected on the basis of global drifts in the image signal (39). We also showed that, with a NA = 1.4 objective lens, focus drifts smaller than 100 nm over three frames (e.g., 30 nm per 1–5 s) have no effect on the mapping of network turnover. Thus, the statistical model described in this section provides a robust method for calculating spatiotemporal maps of assembly and

Figure 2

Relationship between speckle appearance (birth) and disappearance (death) and the turnover in the underlying macromolecular assembly. (*a*) Simulated speckle density in an actin filament network assembling for 120 s and disassembling for 360 s. Inset: Mean intensity indicating the overall change in bound fluorophore over time. (*b*) Classification of speckle birth and death due to monomer association and dissociation with the network. A speckle appears when the difference between foreground (*pink line*) and background (*light blue line*) is greater than a threshold ΔI_C, which is a function of the camera noise and the shot noise of the signal (39). (*c*) Measurement of intensity changes in foreground (*solid pink line*) and background (*solid light blue line*) during a speckle birth. The entire lifetime of the speckle is shown (40 s). Dash-dotted gray line: Mean between foreground and background; error bars: ΔI_C computed in every time point. Birth and death are defined as the time points at which the intensity difference exceeds ΔI_C for the first and the last time. Red line: Regression line to the foreground intensity values before, at, and after birth. Blue dotted line: Regression line to the background intensity values. The cause of speckle birth is inferred by statistical classification of the two slopes and their standard deviations (see text). The statistically more dominant of the two slopes, if also significant relative to image noise, defines the score of the event (foreground slope in the example given). (*d*) Averaging of scores accumulated over a defined time window of a FSM time-lapse sequence yields maps of net polymerization (*red*) and depolymerization (*green*). Scores from birth due to association and death due to dissociation (*d*-i) or from birth due to dissociation and death due to association (*d*-ii) reveal the same distribution of polymerization and depolymerization. Figure in parts reproduced from (39) and from (37) with permission of *Biophysical Journal* and *Science*.

disassembly of macromolecular structures such as F-actin networks.

TIRFM: total internal reflection fluorescence microscopy

Single-Fluorophore Versus Multi-Fluorophore Speckles

It seems that, in many aspects, FSM would be most powerful if implemented as a single-molecule imaging method, where speckle appearances and disappearances unambiguously signal association and dissociation of fluorescent subunits to the platform (55). However, the much simpler signal analysis is counterweighed by several disadvantages not encountered when using multi-fluorophore speckles. First, establishing that an image contains only single-fluorophore speckles can be challenging, especially when the signal of one fluorophore is close to the noise floor of the imaging system. Our experience with single-fluorophore speckles suggests that, particularly in three-dimensional structures, a large fraction of speckles has residual contributions of at least one other fluorophore. Those mixtures need to be deconvolved or eliminated from the statistics. Second, the imaging of single-fluorophore speckles is much more demanding than multi-fluorophore FSM and requires longer camera exposures to capture the very dim signals, reducing the temporal resolution. Third, in addition to the substantially lower temporal resolution, single-fluorophore FSM offers lower spatial resolution because the density of speckles drops significantly with the extremely low labeling ratio. Fourth, multi-fluorophore speckles distinguish between fast and slow turnover, whereas single-fluorophore speckles deliver on/off information only. To measure rates, single-fluorophore speckle analysis must also rely on spatial and temporal averaging, which further decreases the resolution. Watanabe and Mitchison (55) used single-fluorophore speckle analysis to probe actin network turnover in migrating cells with retrograde flow, where most speckles form at the cell edge, move, and then disappear at a distinct site. It remains an open question whether single-fluorophore speckles can characterize the dynamic equilibrium of a spatially stationary or slowly moving network where polymerization and depolymerization coexist over distances less than 1 μm, as achieved by multi-fluorophore speckle analysis (38, 39). It is also unclear whether single-fluorophore speckle analysis has sufficient temporal resolution to extract the short-term components of the dynamic equilibrium.

REQUIREMENTS FOR SPECKLE IMAGING

Time-lapse FSM requires imaging high-resolution diffraction-limited regions containing 1 to 10 fluorophores and inhibiting fluorescence photobleaching. This requires a sensitive imaging system with little extraneous background fluorescence, efficient light collection, a camera with low noise, high quantum efficiency, high dynamic range, high resolution, and suppression of fluorescence photobleaching with illumination shutters and/or oxygen scavengers (30, 58, 64). In addition, all fluorescently labeled molecules must be functionally competent to bind their platform; otherwise they will contribute to diffusible background and obfuscate the speckle contrast (56). We refer the reader to Gupton & Waterman-Storer (17) for a recent in-depth discussion of the hardware requirements for obtaining FSM images.

Because FSM is achieved by the level of fluorescent protein in the sample, it is adaptable to various modes of high-resolution fluorescence microscopy, such that the specific advantages of each mode can be exploited in combination with the quantitative capabilities of FSM. For example, we have performed FSM on both spinning-disk confocal microscope (2) and total internal reflection fluorescence microscope (TIRFM) systems (1) to gain speckle data in two spectral channels with the specific image advantages of confocal and TIRFM. However, to date FSM has proved incompatible with all commercial laser-scanning confocal microscope

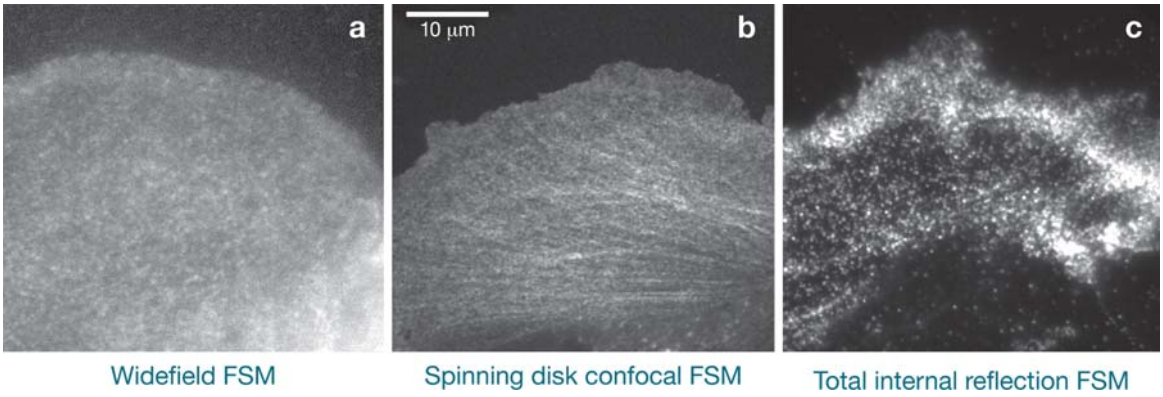

Figure 3

Comparison of X-rhodamine actin FSM images of the edge of migrating Ptk1 epithelial cells using (*a*) wide-field epifluorescence, (*b*) spinning-disk confocal microscopy, and (*c*) total internal reflection fluorescence microscopy. Panels *a* and *b* were acquired using a Nikon 100× 1.4 NA Plan Apo phase contrast objective lens and a 14 bit Hamamatsu Orca II camera with 6.7 micron pixels. Panel *c* was acquired with a Nikon 100× 1.45 NA Plan Apo TIRF objective lens and a 14 bit Hamamatsu Orca II ER with 6.4 micron pixels. Note that speckle contrast and the ability to detect speckles in more central cell regions increases from panels *a* to *c*. Note, however, in the TIRF image that speckles are very bright a few microns back from the edge, likely where the cell is in closer contact with the substrate.

systems available. This is because these instruments use photomultipliers as detectors that are noisy and have a limited dynamic range compared with the low-noise, high dynamic range CCDs used with spinning-disk confocal microscope systems. A comparison of FSM images of the actin cytoskeleton in migrating epithelial cells acquired by wide-field epifluorescence, spinning-disk confocal microscope, and TIRFM is shown in **Figure 3**. Clearly, speckle contrast is improved by reducing out-of-focus fluorescence with either of the last techniques. Contrast in TIRFM images is further improved over the spinning-disk confocal image because the evanescent field excitation depth is reduced to ~50 nm into the specimen. We quantified the effect of the reduced effective imaging volume on modulation and detectability of actin and FA speckles in wide-field epifluorescence and TIRFM. Our analysis showed that TIR-FSM indeed affords major improvements in these parameters over wide-field epifluorescence for imaging macromolecular assemblies at the ventral surface of living cells, both in thin peripheral and thick central cell regions (1).

ANALYSIS OF SPECKLE MOVEMENTS

Tracking Speckle Flow: Early and Recent Developments

In addition to revealing the kinetics of association and dissociation of subunits within a molecular platform, speckles show the movement of the platform. This is evident from raw FSM movies provided as online supplementary material (movies M3 and M4; follow the Supplemental Material link from the Annual Reviews home page at **http://www.annualreviews.org**). The first example shows a speckled actin network, where speckle motion indicates the retrograde flow of the cytoskeleton polymer away from the cell edge. The second example displays speckled microtubules in a meiotic spindle from a *Xenopus laevis* extract. Here, speckles indicate antiparallel, poleward flux of tubulin subunits in the interdigitating microtubule scaffolds of the two half-spindles.

In early applications of FSM, speckle motion was quantified by hand tracking a few speckles, a tedious, error-prone, and

TIR-FSM: total internal reflection fluorescent speckle microscopy

incomplete way of analyzing the wealth of information contained by these images (41, 43, 55). Alternatively, kymographs provided average estimates of speckle velocities (6, 13, 19, 24, 27, 28, 58, 63, 65).

Initial attempts to automate the extraction of more complete speckle flow maps from FSM time-lapse sequences of actin networks relied on correlation-based tracking. The speckled area of a source frame in the movie was divided into small probing windows. Each window was displaced until the normalized cross-correlation of the window with the signal of the target frame, i.e., the next frame in the movie, was maximized. This approach reported the average motion of all the speckles falling into the window. The window size pitted robustness in correlation against spatial resolution. The larger the window, the more unique was the speckle pattern to be recognized in the target frame. On the other hand, larger windows increased the averaging of distinct speckle motions within the window.

Underlying the method of cross-correlation tracking is the assumption that the signal of a probing window, although translocated in space, does not change between source and target frame. In practice, this assumption is always violated because of noise. But, the cross-correlation of two image signals appears to be tolerant toward spatially uncorrelated noise, making it a prime objective function in computer vision tracking (21, 29, 67). The many speckle appearances and disappearances in F-actin networks, however, introduce signal perturbations that cannot be tackled by the cross-correlation function (49). Instead, we developed a particle flow method, in which each speckle was probed separately (49). Speckles were linked between frames by nearest-neighbor assignment in a distance graph, in which conflicts between source speckles competing for the same target speckle were resolved by global optimization (3). Extension of the graph to three frames allowed speckle assignments to be constrained in smooth and unidirectional trajectories, so that speckles moving in antiparallel flow fields could be tracked (49).

Surprisingly, cross-correlation-based tracking was successful in measuring average tubulin flux in mitotic spindles (32). Simulated time-lapse sequences demonstrated that if a significant subpopulation of speckles in the probing window moves jointly, the coherent component of the flow can be estimated even when the rest of the speckles move randomly or, as in the case of the mitotic spindle, a smaller population moves coherently in opposite direction. However, the tracking result will be ambiguous if the window contains multiple, coherently moving speckle subpopulations of equal size. Miyamoto et al. (32) carefully chose windows in the central region of a half-spindle, where the motion of speckles toward the nearer of the two poles dominated speckle motion in the opposite direction and random components. The approach was aided further by several features of the spindle system: Tubulin flux in a spindle is quasi-stationary; speckle appearances and disappearances are concentrated at the spindle midzone and in the pole regions, both of which were excluded from the probing window; and the flow fields were approximately parallel inside the probing window.

Encouraged by these results, we returned to cross-correlation tracking of speckle flow also in F-actin networks (22). The advantage of cross-correlation tracking over particle flow tracking is that there is no requirement to detect the same speckle in at least two consecutive frames. Hence, speckle flows can be tracked in movies with high noise levels and weak speckle contrast (22). To avoid trading correlation stability for spatial resolution, we capitalized on the fact that actin cytoskeleton transport is often stationary on the timescale of minutes. Thus, although the correlation of a single pair of probing windows in source and target frames is ambiguous (**Figure 4*a*-i**), rendering the tracking of speckle flow impossible (**Figure 4*b*-i**), time integration of the correlation function over multiple frame

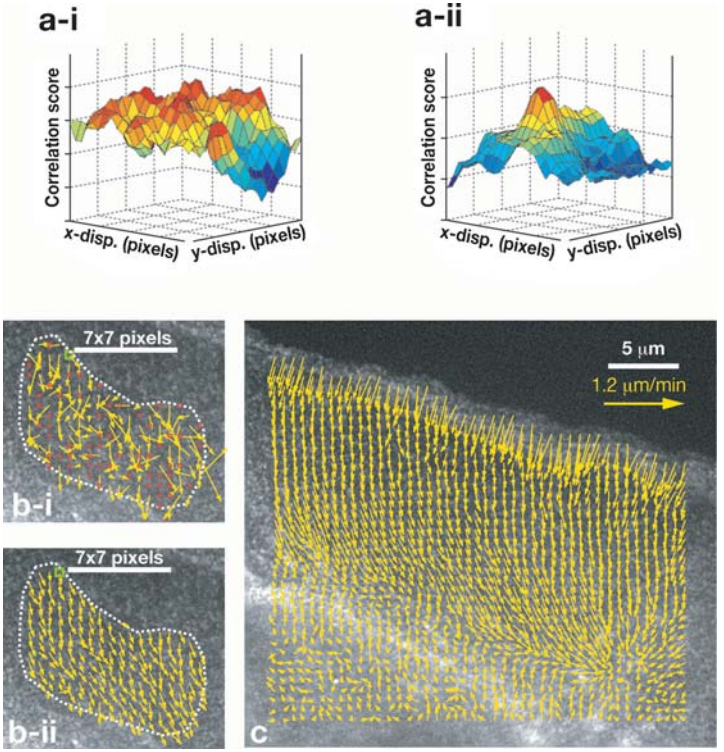

Figure 4

Tracking quasi-stationary speckle flow using multi-frame correlation. (*a*) Cross-correlation for a single frame pair (*a*-i) and for 20 frame pairs integrated (*a*-ii). (*b*) Region of a speckled actin network tracked with a probing window of 7 × 7 pixels (400 × 400 nm) using a single frame pair (*b*-i) and 20 frame pairs (*b*-ii). (*c*) Speckle flow map extracted by integration of the correlation score over 20 frame pairs (movie M3). Speckle flow in this movie is almost stationary, justifying the time integration. Figure reproduced from Reference 22 with permission of *Journal of Microscopy*.

pairs yields robust displacement estimates for probing windows as small as the Airy disk area (**Figure 4*a*-ii**, ***b*-ii**). **Figure 4*c*** presents a complete high-resolution speckle flow map extracted by integration over 20 frames (~3 min).

Tracking Single-Speckle Trajectories

The extraction of kinetic data according to **Figure 3** requires the accurate localization of speckle birth and death events. For this, we had to devise methods capable of tracking full trajectories at the single-speckle level. The large number (>100,000) of dense speckles poses a significant challenge. Details of the current implementation of single-particle tracking of speckles are described by Ponti et al. (38). Our approach follows the framework of most particle-tracking methods, i.e., detection of speckles as particles on a frame-by-frame basis, and the subsequent assignment of corresponding particles in consecutive frames. Assignment is iterated to close gaps in the trajectories created by short-term instability of the speckle signal. Our implementation of this framework includes two algorithms that address particularities of the speckle signal: (*a*) Speckles are detected in an iterative statistical framework, which accounts for signal overlap between proximal speckles. (*b*) Speckle assignments between

consecutive frames are executed in a hybrid approach combining speckle flow and single-speckle tracking. Speckle flow fields are extracted iteratively from previous solutions of single-speckle trajectories and employed to propagate speckle motion between frames prior to establishing the correspondence between thousands of speckle pairs by an efficient numerical implementation of a global nearest-neighbor assignment (4, 8). The very first speckle flow field is obtained by correlation-based tracking (22).

Motion propagation allows us to cope with two problems of FSM data. First, in many cases the magnitude of speckle displacements between two frames significantly exceeds half the distance between speckles. Hence, no solution to the correspondence problem exists without prediction of future speckle locations. Second, speckles undergo sharp spatial gradients in speed and direction of motion. A global propagation scheme discarding regional variations will thus fail, whereas an iterative extraction of the flow field permits a gradually refined trajectory reconstruction in these areas.

Figure 5*a* displays the single-speckle trajectories for speckles initiated in the first 20 frames of the same movie for which speckle flow computation is demonstrated in **Figure 4**. The color-framed close-ups indicate regional differences between trajectories. Window *a*-i contains mostly straight trajectories with an average lifetime of 88 s. The trajectories in window *a*-ii are also straight with an average lifetime of 60 s. In contrast, trajectories in windows *a*-iii and *a*-iv exhibit less directional persistence and have average lifetimes of 65 s and 59 s, respectively. As discussed below, these differences at the level of single-speckle trajectories afforded the segmentation of the cell front into dynamically distinct subregions that correspond to molecularly and functionally distinct actin network modules.

Figure 5*b*,*c* present the steady-state speed of actin network transport and turnover extracted from ~100,000 trajectories. Three different patterns of turnover are recognized that correspond to regions with different average speeds. At the cell edge a ~1-μm-wide band of network assembly (red color; white arrowhead) abuts a ~1-μm-wide band of disassembly (green color; white arrow). The yellow shade in the assembly band indicates that filament polymerization and depolymerization significantly overlap. This 2-μm-wide cell border, which we call the lamellipodium (Lp), exhibits on average the fastest F-actin retrograde flow. Predominant disassembly is found ~10 μm from the cell edge (black arrows), where the speed of F-actin flow is minimal. Here, the retrograde flow of the cell front encounters the anterograde flow of the cell body (B). This region is thus called the convergence zone (C). Between the lamellipodium and the convergence zone is a region called the lamella (L), where assembly and disassembly alternate in a random pattern, accompanied by relatively coherent retrograde flow of moderate speed. The same pattern of network turnover is observed in the cell body.

The high spatial resolution of these turnover maps requires faithful localization of the majority of speckle birth and death events. Trajectory interruptions caused by imprecise tracking introduce pairs of false birth and death events that, unless eliminated by the statistical tests of the score analysis, render inaccurate the measurement of network turnover. Simulated speckle fields with flow characteristics, marker density, and noise similar to real data have demonstrated a 100% success rate of our current single-speckle tracking framework (38). The success of the method on real data cannot be determined because there is no ground truth available. Hand-tracking of speckles is so irreproducible between different operators that the generation of a reliable manual reference data set is impossible. Instead, we demonstrate how incomplete single-speckle trajectories adversely affect the reconstruction of network turnover. **Figure 6*a*** relies on our most current single-speckle tracking package. **Figure 6*b*** presents the

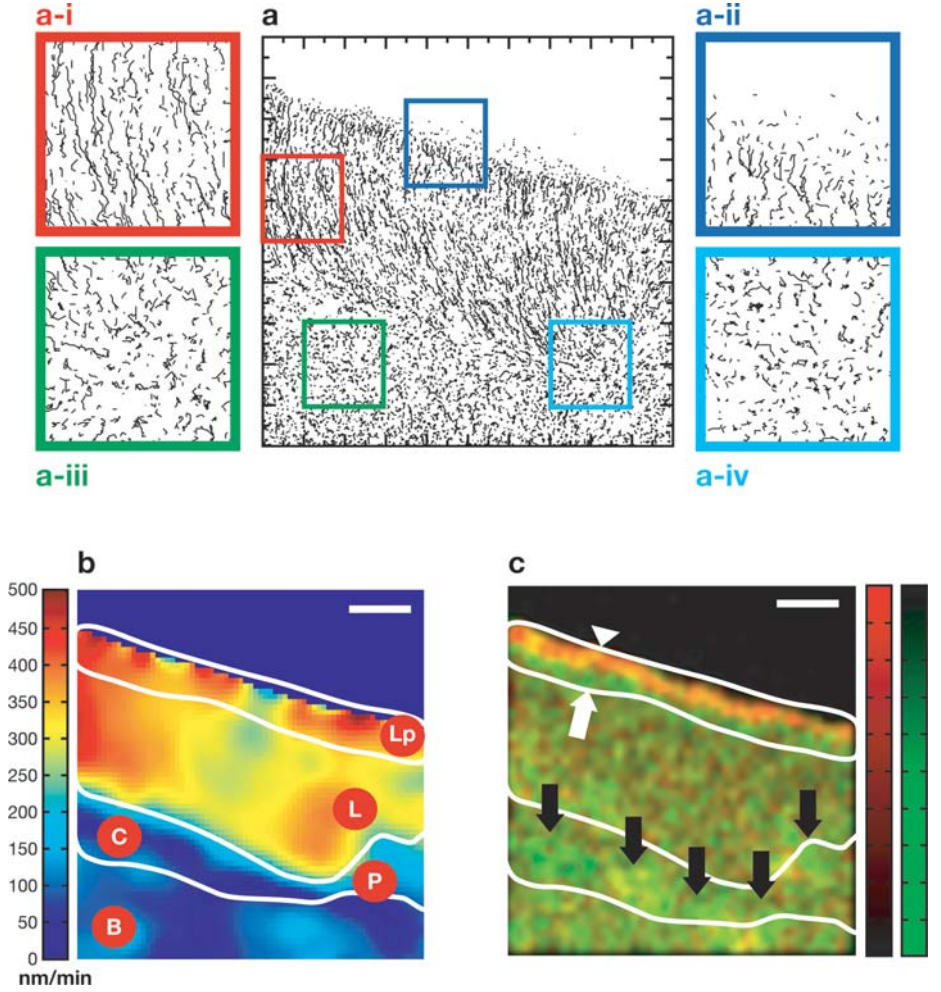

Figure 5

Tracking single-speckle trajectories. (*a*) Trajectories of speckles initiated in the first 20 frames of movie M3. *a*-i to *a*-iv: Close-ups in different areas indicating regional variation in directional persistence, velocity, and lifetime of the trajectories. (*b*) Speed distribution averaged over all 220 frames of the movie. (*c*) Distribution of polymerization (*red channel*) and depolymerization (*green channel*) calculated from scores averaged over 220 frames. Four regions of the actin network with distinct kinematic (motion) and kinetic (turnover) properties can be segmented (see text).

reconstruction of the same turnover map from trajectories tracked without iterative speckle detection and motion propagation. Whereas the maps are similar in large parts of the cell, the less advanced tracking method fails to capture the narrow bands of network assembly and disassembly at the cell edge, where speckles are the densest and a high number of proximate birth and death events confuse the tracking.

Mapping Polymer Turnover Without Speckle Trajectories

It frequently occurs that lower speckle contrast or high image noise do not allow the

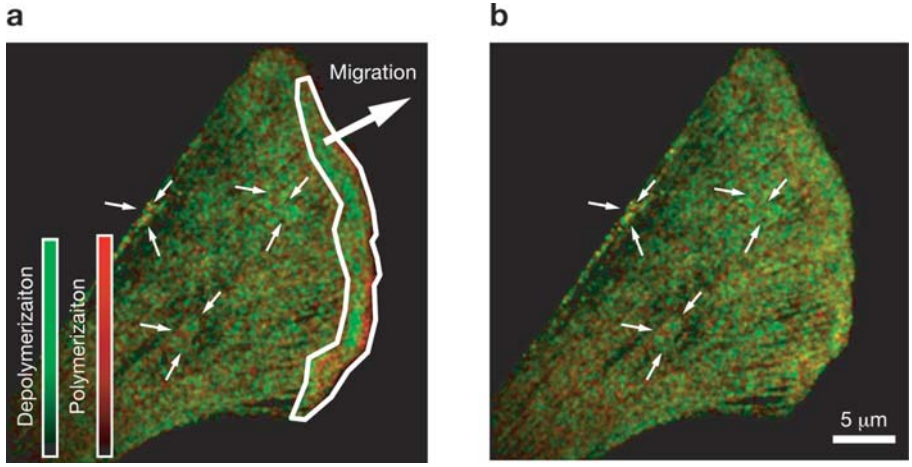

Figure 6

Reconstruction of actin network turnover from trajectories with different tracking quality. (*a*) Application of the model in **Figure 2** to birth and death events determined by the currently most advanced single-speckle tracking method available in our software package. (*b*) Result obtained with a more standard single-particle tracking method that does not include iterative detection of overlapping speckles and motion propagation (see text). Figure reproduced from Reference 22 with permission of *Journal of Microscopy*.

precise identification of single-speckle trajectory endpoints. However, the trackable subsections of the trajectories are usually sufficient to extract the overall structure of speckle flow. In this case an alternative scheme relying on the continuity of the optical density of the speckle field permits the mapping of turnover at lower resolution (48). Shown in **Figure 7**, this method reveals a qualitatively similar organization of actin network assembly and disassembly, but essential features of the turnover patterns that allowed a clear distinction of different regions in **Figure 5*c***, as well as the spatial coexistence of polymerization and depolymerization at the cell edge, are lost with this coarser analysis.

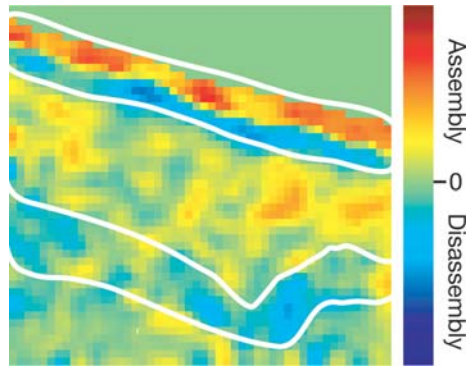

Figure 7

Reconstruction of actin network turnover from speckle flow (**Figure 4*c***) without explicit identification of speckle births and deaths (see text). A spatial organization similar to that in **Figure 5*c*** is mapped; however, essential details in the fine structure of the network turnover are lost. Figure reproduced from Reference 48 with permission of *Proceedings of the National Academy of Sciences, USA*.

APPLICATIONS OF FSM FOR STUDYING PROTEIN DYNAMICS IN VITRO AND IN VIVO

Applications of FSM have thus far focused mostly on the study of actin and microtubule cytoskeleton systems, but other systems have been analyzed with it as well. A summary of the FSM literature can be found in Table S1, which reviews the major

biological findings and highlights technical advances in FSM that have been made in these studies. Most of the FSM data analysis has been limited to kymograph measurements of average speckle flow (see above) and to manual tracking of a few hundred speckles to extract lifetime information (55) and selected trajectories of cytoskeleton structures (19, 41, 43). To our knowledge, in addition to those mentioned in the previous section, few efforts have been made outside our labs to systematically exploit the full spatiotemporal information offered by FSM about transport and turnover in molecular assemblies. The most complete quantitative FSM (qFSM) analyses have so far been performed on F-actin cytoskeleton dynamics in migrating epithelial cells. In the following section we summarize some of the most relevant results of these studies to showcase the technical possibilities of qFSM.

SELECTED RESULTS FROM THE STUDY OF ACTIN IN EPITHELIAL CELL MIGRATION

Organization of Actin Cytoskeleton in Four Kinematically and Kinetically Distinct Regions

Figures 4 and **5** indicate the steady-state organization of the F-actin cytoskeleton in four kinematically and kinetically distinct zones: (*a*) the lamellipodium, characterized by fast retrograde flow and two narrow bands of assembly and disassembly resulting from the fast treadmilling of actin between its polymeric and monomeric states (34, 35); (*b*) the lamella, characterized by reduced retrograde flow and assembly and disassembly in random punctate patterns; (*c*) the cell body, characterized by anterograde flow and turnover patterns similar to those of the lamella; and (*d*) the convergence zone, where the flows of the lamella and cell body meet and where strong depolymerization suggests that the lamella and cell body are materially separate structures.

qFSM also delivers nonsteady-state measurements of flow and turnover, revealing distinct variations in the periodicity of turnover between these regions (38). In combination with pharmacological perturbation, qFSM was used to dissect the mechanisms of retrograde flow. We found that lamellipodium flow is independent of myosin motor contraction, whereas lamella flow is blocked by specific inhibition of myosin II activity (37). Also, the lamellipodium and the lamella exhibited different sensitivity to disruption of filament assembly, disassembly, and severing, suggesting that the regional differences could be associated with differential molecular regulation (37). This hypothesis has thus far been confirmed by immunostaining studies (18, 37) and by expression of constitutively active and dominant negative constructs of regulatory proteins (18; M. Machacek, V. Delorme, G. M. Bokoch, C. M. Waterman-Storer & G. Danuser, unpublished data). Here, qFSM provides a critical insight into cytoskeleton dynamic responses to shifted activation of regulatory factors. In summary, these data demonstrate how qFSM can be used to quantitate spatiotemporal modulations of the kinetics and kinematics of molecular assemblies and to identify dynamically distinct structural modules even when they are composed of the same base protein.

Quantitative fluorescent speckle microscopy (qFSM): combination of FSM with statistical analysis of the speckle signal using specialized qFSM software

Correlation of Actin Assembly with a GFP-p34 Signal Indicates Different Function of the Arp2/3 Complex in Lamellipodium and Lamella

Immunolocalization experiments showed that the lamellipodium is enriched in Arp2/3, a protein complex thought to activate network polymerization by nucleating new filaments off preexisting filaments, and in ADF/cofilin, which promotes filament severing and depolymerization (18, 37). Together, these proteins have been described as mediators of actin treadmilling in the lamellipodium (35). However, Arp2/3 stain was also present in punctate patterns in the lamella. We therefore

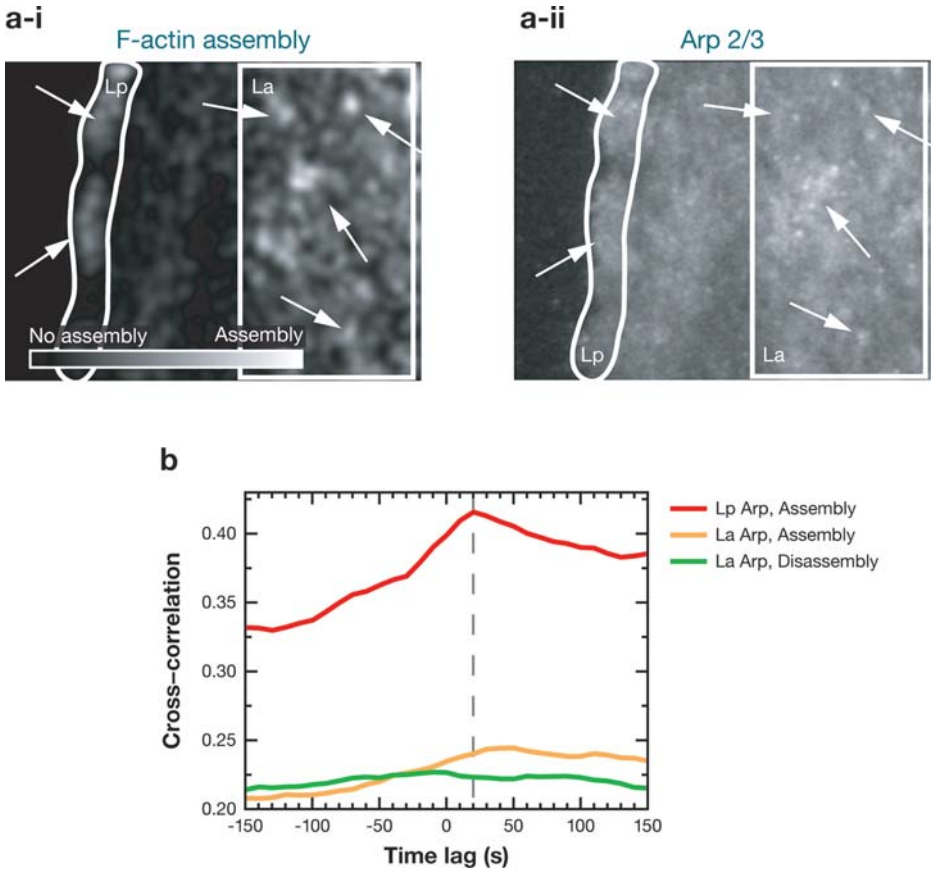

Figure 8

Correlation between actin network assembly, as measured by qFSM, and the signal of the GFP-p34 component of the Arp2/3 complex, a putative regulator of assembly. (*a*) F-actin assembly (*left*) and Arp2/3 distribution (*right*). Arrows point at locations where strong assembly visually correlates with maxima in the Arp2/3 signal. (*b*) Cross-correlations between GFP-p34 signal and assembly in the lamellipodium (*red line*); GFP-p34 signal and assembly in the lamella (*orange line*); and GFP-p34 signal and disassembly in the lamella (*green line*). Figure reproduced from Reference 38 with permission of the *Biophysical Journal*.

speculated that the punctate pattern of lamella assembly could be a direct result of Arp2/3 clustering, as suggested for *Dyctostelium* (5) and yeast (68). To test this hypothesis we correlated time-resolved qFSM F-actin assembly maps with time-lapse image sequences of the GFP-p34 component of the Arp2/3 complex (38). By visual inspection bright signals of net assembly (**Figure 8*a*-i**) appeared to colocalize with bright GFP-p34 signals (**Figure 8*a*-ii**), especially in the lamella (arrows). Cross-correlation of the two maps over time yielded an average correlation of 0.22 with a weak maximum at about +50 s (**Figure 8*b***, orange line). The same correlation was obtained between the GFP-p34 and the disassembly maps (**Figure 8*b***, green line). Simulations of the cross-correlation of random signals confirmed that the correlation value of both comparisons was statistically significant (38). Thus, our data agreed with other studies (5, 68) in that hot spots of lamella network assembly and disassembly tend to colocalize with sites of Arp2/3 accumulation.

Importantly, though, the dynamic analysis revealed the independence of these events in time. This demonstrates the importance of nonsteady-state measurements to probe relationships between molecular processes, as can now be achieved by qFSM.

In the lamellipodium, the cross-correlation between network assembly and GFP-p34 signals was higher and displayed a significant maximum, suggesting a dynamic coupling of F-actin assembly and Arp2/3 aggregation (**Figure 8*b***, red line). The time lag of +20 s implied that the highest rates of assembly precede the maximum of GFP-p34 signal, which is compatible with a model of autocatalytic network assembly by dendritic nucleation (34): A burst of actin polymerization initiates Arp2/3 aggregation by increasing the probability of Arp2/3-mediated filament branching. Increased branching induces exponential network growth until the pool of polymerizable actin monomers is locally depleted. At this point the assembly rate begins to taper off while Arp2/3 continues to associate with preexisting filaments. The peak in Arp2/3 signal is observed when the F-actin network turns from a state of assembly to a state of disassembly. In summary, these data demonstrate how correlating qFSM data with other image cues allows one to examine functional relationships between regulatory factors and the dynamics of effector molecular assemblies.

Coupling of Actin Disassembly and Contraction in the Convergence Zone

A similar spatiotemporal correlation analysis was performed to examine the relationship of actin network depolymerization and contraction in the convergence zone (48). We first established that transient increases in speckle flow convergence are coupled to transient increases in disassembly. This begged the question whether the rate of speckle flow convergence increases because disassembly boosts the efficiency of myosin II motors in contracting a more compliant network or because motor contraction mediates network disassembly. To address this question, we transiently perfused cells with calyculin A, a type II phosphatase inhibitor that increases myosin II activity. Unexpectedly, we reproducibly measured a strong burst of disassembly long before flow convergence was affected. This evidence suggested that myosin II contraction can actively promote depolymerization of F-actin, for example, by breaking filaments. The link between F-actin contractility and turnover has since been confirmed by fluorescence recovery after photobleaching measurements in the contractile ring required for cytokinesis (33). In summary, these data demonstrate the correlation of two qFSM parameters to decipher the relationship between deformation and plasticity of polymer networks inside cells.

Heterogeneity in Speckle Velocity and Lifetime Reveals Spatial Overlap of Lamellipodium and Lamella at the Leading Edge

The transition between the lamellipodium and the lamella is characterized by a narrow band of strong disassembly adjacent to a region of mixed assembly and disassembly and a sharp decrease in retrograde flow velocity (**Figure 5**). Together, these features defined a unique mathematical signature for tracking the boundary between the two regions over time (**Figure 9*a***). In view of the differences of speckle velocities and lifetime between the two regions, we speculated that the same boundary could be tracked by spatial clustering of speckle properties. We predicted that fast, short-living speckles (class 1) would preferentially localize in the lamellipodium, whereas slow, longer-living speckles (class 2) would be dominant in the lamella. To test this hypothesis, we solved a multiobjective optimization problem in which the thresholds of velocity v_{th} and lifetime τ_{th} separating the two classes, as well as the boundary ∂Lp between lamellipodium and lamella,

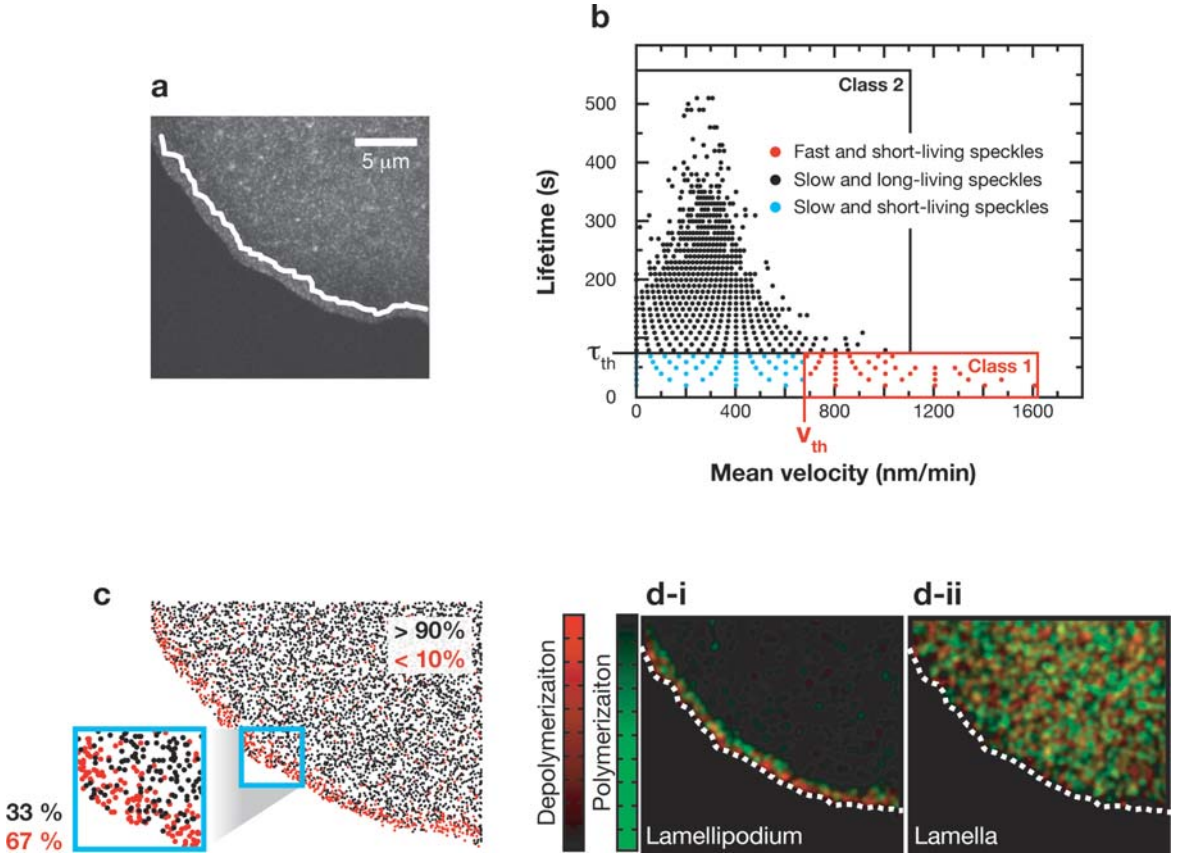

Figure 9

Distinction of two spatially overlapping actin networks based on heterogeneity of single-speckle properties. (*a*) Raw FSM image overlaid with the boundary between lamellipodium and lamella computed from spatial gradients in actin turnover and flow velocity. Animation of this data is provided in movie M5 (follow the Supplemental Material link from the Annual Reviews home page at **http://www.annualreviews.org**). (*b*, *c*) Cluster analysis of speckle lifetime and velocity (see text). (*d*) Class 1 speckles constitute the rapidly treadmilling lamellipodium. Class 2 speckles constitute the lamella with a punctate pattern of random actin turnover. Both networks spatially overlap in the first 2 μm from the cell edge.

were determined subject to the rule $\{\partial \mathrm{Lp}, \tau_{\mathrm{th}}, v_{\mathrm{th}}\} = \max(N_1/(N_1 + N_2) \in \mathrm{Lp}) \,\&\, \min(N_1/(N_1 + N_2) \in \mathrm{La})$ (**Figure 9*b***). N_1 and N_2 denote the number of speckles in classes 1 and 2, respectively. Our prediction was confirmed in the lamella, where class 1 speckles occupied a statistically insignificant fraction. However, class 2 speckles made up 30% to 40% of the lamellipodium, indicating that in this region speckles with different kinetic and kinematic behavior colocalize. This information was previously lost in the averaged analysis of single-speckle trajectories. When mapping the scores of class 1 and class 2 speckles separately, we discovered that class 1 speckles define the bands of polymerization and depolymerization characteristic of the lamellipodium and that class 2 speckles define the puncta of assembly and disassembly characteristic of the lamella, which reaches all the way to the leading edge. Subsequent experiments

specifically disrupting actin treadmilling in the lamellipodium confirmed our finding that the lamellipodium and lamella form two spatially overlapping yet kinetically, kinematically, and molecularly different actin networks (18, 37).

In summary, these data exemplify that qFSM analysis has come to the level at which single-speckle properties can be exploited to probe the heterogeneity of molecular assemblies in space and time.

NEW APPLICATIONS OF FSM

Two-Speckle Microrheology Probes Viscoelastic Properties of Actin Networks

Speckle trajectories probe different dynamic phenomena at different spatial and temporal scales. So far we have exploited the long-range, directed components of trajectories to extract the flow and deformation of F-actin networks induced by molecular forces coordinated over several microns, e.g., the activity of a large number of myosin II motors in the convergence zone. On a shorter spatiotemporal scale, speckle trajectories contain components associated with microscopic deformations of the network that are induced by less coordinated local contractions of small

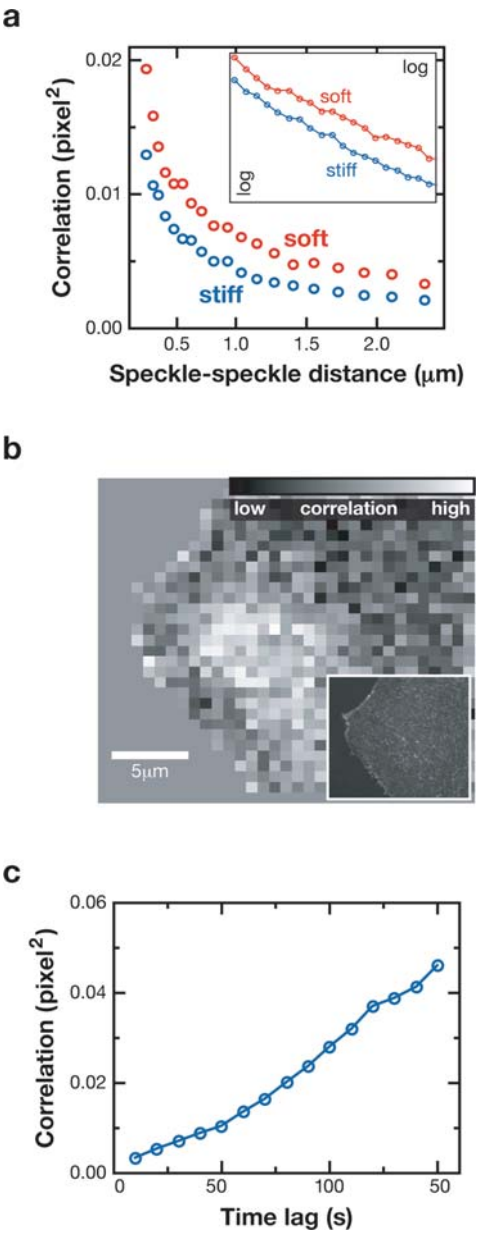

Figure 10

Two-speckle microrheology of F-actin network stiffness inside cells. (*a*) Correlation of random motion of two speckles as a function of their distance *r*. The curves follow a $1/r$ decay (see inset), as is predicted for a viscoelastic medium. (*b*) Spatial mapping of correlation values. The correlation landscape has a smooth spatial variation at length scales much longer than the size of one probing window. This suggests that regional heterogeneity is not due to noise. (*c*) Correlation as a function of the time lag over which speckle displacements are determined. The linearity of the curve indicates that the correlation is dominated by diffusive motion, which permits direct conversion of the correlation values into parameters describing the viscoelasticity of F-actin networks.

myosin patches (50) and thermal forces. Also, positional fluctuations of speckles relate to the sliding of decoupled filaments, filament bending inside the network, and photometric shifts of the speckle centroids induced by local fluorophore exchange. These fluctuations occur at a length scale shorter than the mesh size of the network and/or are

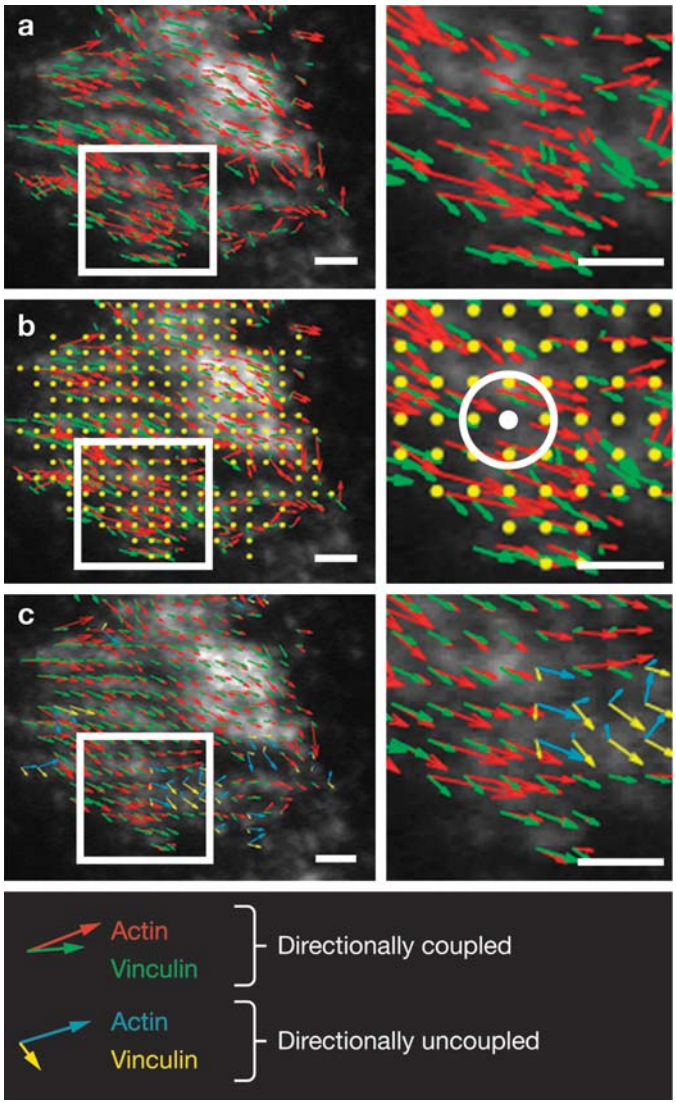

Figure 11

Correlative, multispectral qFSM analysis of F-actin and vinculin. (*a–c*) Processing steps in the measurement of the coupling of F-actin (*red vectors*) and vinculin (*green vectors*) flows, overlaid to the raw speckle image of vinculin (see text for further discussion). Blue (actin) and yellow (vinculin) vectors in panel *c* indicate a region where the two molecules are directionally decoupled. Scale bar: 5 μm.

independent between speckles. When calculating the cross-correlation of trajectories of two speckles separated by a distance greater than the mesh size of the network, these fluctuations cancel out. However, even after directional components are eliminated, the cross-correlation between two-speckle trajectories decays with $1/r$, where r denotes the distance between them (**Figure 10*a***). This behavior is known from two-point microrheology, in which embedded beads instead of speckles are used to track thermal fluctuations in polymer networks (9, 14). Thus, spatially correlated yet undirected components of speckle motion could be used to probe material properties of polymer networks inside a cell with a resolution at the scale of the interspeckle distance.

This possibility capitalizes on recent enhancements of speckle tracking to an accuracy of approximately one tenth of a pixel even when speckles overlap. Also, we implemented a module that performs correlation analysis in small windows to map out the spatial modulation of material properties (**Figure 10*b***). Whereas in a noncontractile polymer network this map would directly reveal spatial variation of network stiffness, the inhomogeneity could also be the result of spatially variable motor activity. To test for this possibility we computed the correlation as a function of the time over which speckle displacements are tracked. For purely thermal fluctuations the relationship between cross-correlation magnitude and time is linear, whereas for a motor-driven fluctuation one would expect superdiffusive speckle motion (42). **Figure 10*c*** shows that for a time range of 5 to 50 s the relationship is indeed linear. Thus, **Figure 10*b*** may provide a first glimpse of the variation of the stiffness of F-actin networks at the micron scale.

Correlational qFSM of the Dynamic Engagement of Actin Cytoskeleton and Focal Adhesions

We have begun to extend our particle-tracking-based analysis of speckles in one spectral channel to correlative particle tracking in two spectrally distinct channels with the goal of analyzing the kinematic coupling between two macromolecular assemblies. We

used this approach to derive initial models of the coupling of the F-actin cytoskeleton to FA proteins in migrating epithelial cells. **Figure 11** illustrates the steps of correlational qFSM on dual-channel TIR-FSM images of F-actin and vinculin speckles. Single-speckle tracking was first applied separately to both channels (**Figure 11*a***). Speckle flows were then mapped onto a common grid to allow comparison of pairs of speckles between the two channels (**Figure 11*b***). Speckle assignment to the closest local grid position is achieved with distance-weighted, locally adaptive interpolation (white circle). Following grid assignment, the correlation between the direction and speed of speckle flow vectors was computed. To quantitate the kinematic coupling of actin and FA molecules, two metrics are currently used. A direction correlation score ranging from –1 to 1 is defined as the cosine of the angle between the two vectors at any one grid point (**Figure 11*c***). A speed correlation score is defined as $(\Sigma\ v_{FA} \perp v_{act})/|v_{act}|$, where $(\Sigma\ v_{FA} \perp v_{act})$ denotes the average of the velocity projection of the FA flow field onto the actin vector flow axis, and $|v_{act}|$ is the magnitude average of actin vectors. This value thus represents how the speed of FA molecules along the actin axis compares with the speed of F-actin itself. For two identical flow fields, both the direction and speed correlation scores are 1.

Preliminary correlational qFSM studies have already revealed thus far unknown patterns of molecular coupling to FAs. For example, we found a low degree of kinematic coupling between F-actin and the FA proteins integrin, FAK, zyxin, and paxillin, as indicated by low direction and speed correlation scores. In contrast, our analysis revealed a high degree of kinematic coupling between F-actin flow and FA proteins α-actinin, talin, and vinculin. This indicates the power of correlational qFSM for spatiotemporally quantifying the degree of engagement of pairs of colocalized molecules in subcellular macromolecular assemblies.

CONCLUSION

Over the past few years FSM has been advanced to a versatile tool for simultaneously probing the motion, deformation, turnover, and material properties of macromolecular assemblies. In a next step, these parameters will be combined in correlational analyses to establish how assemblies operate as dynamic and plastic structures, enabling a broad variety of cell functions. In parallel, FSM will go multispectral, so that these parameters can be correlated among different macromolecular structures. This requires major modifications to the current qFSM software to cope with the explosion of combinatorial data in two or more simultaneously imaged speckle channels.

Despite the conceptual simplicity, FSM has remained an expert technique used by a relatively small number of research laboratories. Two measures will be taken by our labs in an attempt to spread FSM as a routine mode of light microscopy. First, protocols are under development to generate cell lines that permanently express low levels of fluorescent cytoskeleton proteins optimized for speckle image formation. This will avoid the time-consuming steps of microinjection and the tweaking of transient expression of fluorescent protein and will turn FSM into a robust technique with high quantitative reproducibility. Second, the qFSM software package will be released. The use of cell lines with reproducible levels of fluorescent protein will greatly aid the software distribution. Under standardized conditions many of the processing steps can be furnished with default control parameters so that meaningful results can be obtained without in-depth knowledge of the mathematical algorithms.

Last, the idea of FSM will be promoted by more applications outside the cytoskeleton field. The analyses of FA dynamics make an initial step in this direction. Projects are underway to apply qFSM to studies of the dynamic interaction of clathrin, dynamin,

and actin structures during endocytosis, and of DNA repair. Despite the many existing discoveries already made by FSM, as documented by the sizable list of publications in Table S1, it is still a technology in the infancy of its uses.

ACKNOWLEDGMENTS

This research is supported by NIH through the grant R01 GM67230 to C.W.S. and G.D. We are grateful to Ke Hu, Lin Ji, Stephanie Gupton, and Dinah Loerke for sharing unpublished data; and to Kathryn Thompson for a careful reading of the manuscript.

LITERATURE CITED

1. Guidelines for the practical implementation of a total internal reflection light microscope amenable to FSM.

2. Guidelines for the practical implementation of a spinning disk confocal microscope amenable to FSM.

7. Application of FSM to study the transient association of a cytoskeleton-binding protein with the cytoskeleton.

1. **Adams M, Matov A, Yarar D, Gupton S, Danuser G, Waterman-Storer CM. 2004. Signal analysis of total internal reflection fluorescent speckle microscopy (TIR-FSM) and widefield epi-fluorescence FSM of the actin cytoskeleton and focal adhesions in living cells. *J. Microsc.* 216:138–52**
2. **Adams MC, Salmon WC, Gupton SL, Cohan CS, Wittmann T, et al. 2003. A high-speed multispectral spinning-disk confocal microscope system for fluorescent speckle microscopy of living cells. *Methods* 29:29–41**
3. Ahuja RK, Magnanti TM, Orlin JB. 1993. *Network Flows: Theory, Algorithms and Optimization*. Saddle River, NJ: Prentice-Hall. 846 pp.
4. Blackman SS, Popoli R. 1999. *Design and Analysis of Modern Tracking Systems*. Noorwood, MA: Artech House
5. Bretschneider T, Diez S, Anderson K, Heuser JA, Clarke M, et al. 2004. Dynamic actin patterns and Arp2/3 assembly at the substrate-attached surface of motile cells. *Curr. Biol.* 14:1–10
6. Brust-Mascher I, Scholey JM. 2002. Microtubule flux and sliding in mitotic spindles of *Drosophila* embryos. *Mol. Biol. Cell* 13:3967–75
7. **Bulinski JC, Odde DJ, Howell BJ, Salmon TD, Waterman-Storer CM. 2001. Rapid dynamics of the microtubule binding of ensconsin *in vivo*. *J. Cell Sci.* 114:3885–97**
8. Burkard KE, Cela E. 1999. Linear assignment problems and extensions. In *Handbook of Combinatorial Optimization*, ed. DZ Du, PM Pardalos, pp. 75–149. Dordrecht: Kluwer Acad. Publ.
9. Crocker JC, Valentine MT, Weeks ER, Gisler T, Kaplan PD, et al. 2000. Two-point microrheology of inhomogeneous soft materials. *Phys. Rev. Lett.* 85:888–91
10. Danuser G, Waterman-Storer CM. 2003. Fluorescent speckle microscopy: where it came from and where it is going. *J. Microsc.* 211:191–207
11. Desai A, Mitchison TJ. 1997. Microtubule polymerization dynamics. *Annu. Rev. Cell Dev. Biol.* 13:83–117
12. Dunn GA, Dobbie IM, Monypenny J, Holt MR, Zicha D. 2002. Fluorescence localization after photobleaching (FLAP): a new method for studying protein dynamics in living cells. *J. Microsc.* 205:109–12
13. Gaetz J, Kapoor TM. 2004. Dynein/dynactin regulate metaphase spindle length by targeting depolymerizing activities to spindle poles. *J. Cell Biol.* 166:465–71
14. Gardel ML, Shin JH, MacKintosh FC, Mahadevan L, Matsudaira P, Weitz DA. 2004. Elastic behavior of cross-linked and bundled actin networks. *Science* 304:1301–5
15. Geiger B, Bershadsky A, Pankov R, Yamada KM. 2001. Transmembrane extracellular matrix-cytoskeleton crosstalk. *Nat. Rev. Mol. Cell Biol.* 2:793–805

16. Grego S, Cantillana V, Salmon ED. 2001. Microtubule treadmilling *in vitro* investigated by fluorescence speckle and confocal microscopy. *Biophys. J.* 81:66–78
17. Gupton S, Waterman-Storer CM. 2006. Live-cell fluorescent speckle microscopy (FSM) of actin cytoskeletal dynamics and their perturbation by drug perfusion. In *Cell Biology: A Laboratory Handbook*, ed. J Celis, JV Small, pp. 137–51. Amsterdam: Elsevier
18. Gupton SL, Anderson KL, Kole TP, Fischer RS, Ponti A, et al. 2005. Cell migration without a lamellipodium: translation of actin dynamics into cell movement mediated by tropomyosin. *J. Cell Biol.* 168:619–31
19. Gupton SL, Salmon WC, Waterman-Storer CM. 2002. Converging populations of F-actin promote breakage of associated microtubules to spatially regulate microtubule turnover in migrating cells. *Curr. Biol.* 12:1891–99
20. Inoue S, Spring KR. 1997. *Video Microscopy: The Fundamentals*. New York/London: Plenum. 764 pp.
21. Jepson AD, Fleet DJ, El-Maraghi TF. 2003. Robust online appearance models for visual tracking. *IEEE Trans. Pattern Anal. Mach. Intell.* 25:1296–311
22. Ji L, Danuser G. 2005. Tracking quasi-stationary flow of weak fluorescent features by multi-frame correlation. *J. Microsc.* 220:150–67
23. Jurado C, Haserick JR, Lee J. 2005. Slipping or gripping? Fluorescent speckle microscopy in fish keratocytes reveals two different mechanisms for generating a retrograde flow of actin. *Mol. Biol. Cell* 16:507–18
24. Kapoor TM, Mitchison TJ. 2001. Eg5 is static in bipolar spindles relative to tubulin: evidence for a static spindle matrix. *J. Cell Biol.* 154:1125–34
25. Lippincott-Schwartz J, Patterson GH. 2003. Development and use of fluorescent protein markers in living cells. *Science* 300:87–91
26. Luby-Phelps K. 2000. Cytoarchitecture and physical properties of cytoplasm: volume, viscosity, diffusion, intracellular surface area. *Int. Rev. Cytol.* 192:189–221
27. Maddox P, Desai A, Oegema K, Mitchison TJ, Salmon ED. 2002. Poleward microtubule flux is a major component of spindle dynamics and anaphase A in mitotic *Drosophila* embryos. *Curr. Biol.* 12:1670–74
28. Maddox P, Straight A, Coughlin P, Mitchison TJ, Salmon ED. 2003. Direct observation of microtubule dynamics at kinetochores in *Xenopus* extract spindles: implications for spindle mechanics. *J. Cell Biol.* 162:377–82
29. Micheli ED, Torre V, Uras S. 1993. The accuracy of the computation of optical flow and of the recovery of motion parameters. *IEEE Trans. Pattern Anal. Mach. Intell.* 15:434–47
30. Mikhailov AV, Gundersen GG. 1995. Centripetal transport of microtubules in motile cells. *Cell Motil. Cytoskelet.* 32:173–86
31. Mitchison TJ. 1989. Polewards microtubule flux in the mitotic spindle: evidence from photoactivation of fluorescence. *J. Cell Biol.* 109:637–52
32. Miyamoto DT, Perlman ZE, Burbank KS, Groen AC, Mitchison TJ. 2004. The kinesin Eg5 drives poleward microtubule flux in *Xenopus laevis* egg extract spindles. *J. Cell Biol.* 167:813–18
33. Murthy K, Wadsworth P. 2005. Myosin-II-dependent localization and dynamics of F-actin during cytokinesis. *Curr. Biol.* 15:724–31
34. Pollard TD, Blanchoin L, Mullins RD. 2000. Molecular mechanisms controlling actin filament dynamics in nonmuscle cells. *Annu. Rev. Biophys. Biomol. Struct.* 29:545–76
35. Pollard TD, Borisy GB. 2003. Cellular motility driven by assembly and disassembly of actin filaments. *Cell* 112:453–65

17. Guidelines for the preparation of live cell samples for FSM and for the realization of perfusion chambers that allow the transient application of small-molecule inhibitors of cytoskeleton functions during FSM imaging.

36. Ponti A. 2004. *High-Resolution Analysis of F-Actin Meshwork Kinetics and Kinematics Using Computational Fluorescent Speckle Microscopy*. Zurich: ETH. 185 pp.

37. Ponti A, Machacek M, Gupton SL, Waterman-Storer CM, Danuser G. 2004. Two distinct actin networks drive the protrusion of migrating cells. *Science* 305:1782–86

38. Ponti A, Matov A, Adams M, Gupton S, Waterman-Storer CM, Danuser G. 2005. Periodic patterns of actin turnover in lamellipodia and lamellae of migrating epithelial cells analyzed by quantitative fluorescent speckle microscopy. *Biophys. J.* 89:3456–69

39. Ponti A, Vallotton P, Salmon WC, Waterman-Storer CM, Danuser G. 2003. Computational analysis of F-actin turnover in cortical actin meshworks using fluorescent speckle microscopy. *Biophys. J.* 84:3336–52

40. Prasher DC. 1995. Using GFP to see the light. *Trends Genet.* 11:320–23

41. Salmon WC, Adams MC, Waterman-Storer CM. 2002. Dual-wavelength fluorescent speckle microscopy reveals coupling of microtubule and actin movements in migrating cells. *J. Cell Biol.* 158:31–37

42. Saxton MJ, Jacobson K. 1997. Single-particle tracking: application to membrane dynamics. *Annu. Rev. Biophys. Biomol. Struct.* 26:373–99

43. Schaefer AW, Kabir N, Forscher P. 2002. Filopodia and actin arcs guide the assembly and transport of two populations of microtubules with unique dynamic parameters in neuronal growth cones. *J. Cell Biol.* 158:139–52

44. Small V. 1981. Organization of actin in the leading edge of cultured cells. *J. Cell Biol.* 91:695–705

45. Svitkina TM, Verkhovsky AB, McQuade KM, Borisy GG. 1997. Analysis of the actin-myosin II system in fish epidermal keratocytes: mechanism of cell body translocation. *J. Cell Biol.* 139:397–415

46. Theriot JA, Mitchison TJ. 1991. Actin microfilament dynamics in locomoting cells. *Nature* 352:126–31

47. Vallotton P, Danuser G, Bohnet S, Meister JJ, Verkhovsky A. 2005. Retrograde flow in keratocytes: news from the front. *Mol. Biol. Cell* 16:1223–31

48. Vallotton P, Gupton SL, Waterman-Storer CM, Danuser G. 2004. Simultaneous mapping of filamentous actin flow and turnover in migrating cells by quantitative fluorescent speckle microscopy. *Proc. Natl. Acad. Sci. USA* 101:9660–65

49. Vallotton P, Ponti A, Waterman-Storer CM, Salmon ED, Danuser G. 2003. Recovery, visualization, and analysis of actin and tubulin polymer flow in live cells: a fluorescence speckle microscopy study. *Biophys. J.* 85:1289–306

50. Verkhovsky AB, Svitkina TM, Borisy GG. 1999. Network contraction model for cell translocation and retrograde flow. In *Cell Behaviour: Control and Mechanism of Motility*, ed. JM Lackie, GA Dunn, GE Jones, pp. 207–22. London: Portland

51. Verkhovsky AB, Svitkina TM, Borisy GG. 1999. Self-polarization and directional motility of cytoplasm. *Curr. Biol.* 9:11–20

52. Wadsworth P, Salmon E. 1986. Analysis of the treadmilling model during metaphase of mitosis using fluorescence redistribution after photobleaching. *J. Cell Biol.* 102:1032–38

53. Wang Y. 1985. Exchange of actin subunits at the leading edge of living fibroblasts: possible role of treadmilling. *J. Cell Biol.* 101:597–602

54. Wang YL, Heiple JM, Taylor DL. 1982. Fluorescent analog cytochemistry of contractile proteins. *Methods Cell Biol.* 25:1–11

55. Watanabe Y, Mitchison TJ. 2002. Single-molecule speckle analysis of actin filament turnover in lamellipodia. *Science* 295:1083–86

37. Discovery of two dynamically and molecularly distinct yet spatially overlapping actin cytoskeleton structures in epithelial cells using cluster analysis of single-speckle properties.

39. Statistical model for the extraction of rates of polymer assembly and disassembly by classification of intensity changes during speckle appearance and disappearance events.

41. Application of two-color FSM to examine the interaction of the actin and microtubule cytoskeletons in epithelial cell migration.

43. Application of two-color FSM to examine the interaction of the actin and microtubule cytoskeletons in neuronal growth cones.

55. Imaging and analysis of single-fluorophore speckles to probe actin cytoskeleton dynamics during cell motility.

56. Waterman-Storer CM. 2002. Fluorescent speckle microscopy (FSM) of microtubules and actin in living cells. In *Current Protocols in Cell Biology*, ed. JS Bonifacino, M Dasso, JB Harford, J Lippincott-Schwartz, KM Yamada, Unit 4.10. New York: Wiley
57. Waterman-Storer CM, Danuser G. 2002. New direction of fluorescent speckle microscopy. *Curr. Biol.* 12:R633–R40
58. Waterman-Storer CM, Desai A, Bulinski JC, Salmon ED. 1998. Fluorescent speckle microscopy, a method to visualize the dynamics of protein assemblies in living cells. *Curr. Biol.* 8:1227–30
59. Waterman-Storer CM, Desai A, Salmon ED. 1999. Fluorescent speckle microscopy of spindle microtubule assembly and motility in living cells. *Methods Cell Biol.* 61:155–73
60. Waterman-Storer CM, Salmon ED. 1997. Actomyosin-based retrograde flow of microtubules in the lamella of migrating epithelial cells influences microtubule dynamic instability and turnover and is associated with microtubule breakage and treadmilling. *J. Cell Biol.* 139:417–34
61. Waterman-Storer CM, Salmon ED. 1998. How microtubules get fluorescent speckles. *Biophys. J.* 75:2059–69
62. Waterman-Storer CM, Salmon ED. 1999. Fluorescent speckle microscopy of MTs: How low can you go? *FASEB J.* 13:225–30
63. Waterman-Storer CM, Salmon WC, Salmon ED. 2000. Feedback interactions between cell-cell adherens junctions and cytoskeletal dynamics in newt lung epithelial cells. *Mol. Biol. Cell* 11:2471–83
64. Waterman-Storer CM, Sanger JW, Sanger JM. 1993. Dynamics of organelles in the mitotic spindles of living cells: membrane and microtubule interactions. *Cell Motil. Cytoskelet.* 26:19–39
65. Wittmann T, Bokoch GM, Waterman-Storer CM. 2003. Regulation of leading edge microtubule and actin dynamics downstream of Rac1. *J. Cell Biol.* 161:845–51
66. Wolf DE. 1989. Designing, building, and using a fluorescence recovery after photobleaching instrument. *Methods Cell Biol.* 30:271–306
67. Ye M, Haralick RM, Shapiro LG. 2003. Estimating piecewise-smooth optical flow with global matching and graduated optimization. *IEEE Trans. Pattern Anal. Mach. Intell.* 25:1625–30
68. Young ME, Cooper JA, Bridgman PC. 2004. Yeast actin patches are networks of branched actin filaments. *J. Cell Biol.* 166:629–35
69. Zhang X-F, Schaefer AW, Burnette DT, Schoonderwoert VT, Forscher P. 2003. Rho-dependent contractile responses in the neuronal growth cone are independent of classical peripheral retrograde actin flow. *Neuron* 40:931–44
70. Zicha D, Dobbie IM, Holt MR, Monypenny J, Soong DYH, et al. 2003. Rapid actin transport during cell protrusion. *Science* 300:142–45

61. Definition and analysis of the stochastic assembly model of how microtubules get speckles.

Annual Review of Biophysics and Biomolecular Structure

Volume 35, 2006

Contents